SOFT ROBOTICS
Volume 00, Number 00, 2018

DOI: 10.1089/soro.2018.0065

SoRo
Soft Robotics

Soft Poly-Limbs: Toward a New Paradigm of Mobile Manipulation for Daily Living Tasks

Pham Huy Nguyen,[1] Curtis Sparks,[1] Sai G. Nuthi,[2] Nicholas M. Vale,[3] and Panagiotis Polygerinos[1]

Abstract

We present the design and development of the fluid-driven, wearable, Soft Poly-Limb (SPL), from the Greek word *polys*, meaning many. The SPL utilizes the numerous traits of soft robotics to enable a novel approach in providing safe and compliant mobile manipulation assistance to healthy and impaired users. This wearable system equips the user with a controllable additional limb that is capable of complex three-dimensional motion in space. Similar to an elephant trunk, the SPL is able to manipulate objects using a variety of end effectors, such as suction adhesion or a soft grasper, as well as its entire soft body to conform around an object, able to lift 2.35 times its own weight. To develop these highly articulated soft robotic limbs, we provide a novel set of systematic design rules, obtained through varying geometrical parameters of the SPL through experimentally verified finite element method models. We investigate performance of the limb by testing the lifetime of the new SPL actuators, evaluating its payload capacity, operational workspace, and capability of interacting close to a user through a spatial mobility test. Furthermore, we are able to demonstrate limb controllability through multiple user-intent detection modalities. Finally, we explore the limb's ability to assist in multitasking and pick and place scenarios with varying mounting locations of the SPL around the user's body. Our results highlight the SPL's ability to safely interact with the user while demonstrating promising performance in assisting with a wide variety of tasks, in both work and general living settings.

Keywords: soft actuator, soft poly-limb, wearable, continuum, finite element modeling, ring-reinforced actuator

Introduction

Robotic manipulators that can be worn on the human body provide users with extra appendages to support, assist, or enhance their existing capabilities. Such wearable manipulators do not aim at replacing biological limbs such as prosthetic devices[1] or provide musculoskeletal augmentation such as exoskeletons.[2] Kinematically, these robots do not have to follow the user's anatomy and therefore do not restrict movement or require alignment with biological joints, and are easier to don and doff. Examples of wearable manipulators have ranged from robotic arms,[3,4] legs,[5,6] and fingers,[7–9] showing functional benefits in industrial[3] and medical[9,10] tasks.

However, the introduction of wearable manipulators brings up the question of adoption and controllability. Previous research has shown that the human central nervous system is capable of accepting and learning to control additional limbs.[11,12] Therefore, with some training, humans should be capable of working with additional limbs to complete tasks more effectively. Preliminary research has shown controllability of robotic manipulators with multiple human participants, utilizing biological signals from the frontalis muscle on the forehead,[13] torso muscles,[14] the foot,[15] or the elbow.[8] Additional forms of user-intent detection to control robot manipulators that work closely to humans have been documented.[16–19] Nevertheless, adoption of such devices goes beyond just being able to control them. There are psychological and social factors involved, for example the stigma of having additional limbs as seen in people with Polymelia (people or animals with more than usual number of biological limbs).[20–23] In recent studies,[4,24] focus groups have been assembled to expand on the possible use cases and the viability of wearable manipulators. In terms of adoption, the majority of the focus groups received wearable manipulators

[1]The Polytechnic School, Ira A. Fulton Schools of Engineering, Arizona State University, Mesa, Arizona.
[2]The School for Engineering of Matter, Transport and Energy, Ira A. Fulton Schools of Engineering, Arizona State University, Tempe, Arizona.
[3]The School of Biological Health Systems Engineering, Ira A. Fulton Schools of Engineering, Arizona State University, Tempe, Arizona.

and their capabilities favorably and even requested personalizable features such as different colors and designs. Additionally, the focus groups preferred robotesque limbs over anthropomorphic limbs, suggesting that the latter would be ''creepy'' or ''scary.'' A need for a comfortable, easy to don and doff, and lightweight robot was also expressed.

Although the benefits from the use of wearable manipulators are slowly becoming more apparent, most of the current robotic systems still have to face the obstacles that come with their rigid design, such as weight, size, and the challenging interaction between human tissue and rigid materials.[25] These challenges lead to questions related to the safety of the user that could possibly limit technological, and later social, adoption. One of the emerging solutions to tackle these challenges originates from soft robotics. Soft robots, or intrinsically soft devices, are highly adaptable and robust to the changing environment, safe for human–robot interaction, low cost in terms of fabrication, lightweight, and finally offer high power-to-weight ratios.[26–29] Their compliant nature allows conformity to the user's body without causing tissue damage, making them suitable for wearable applications.[30–36] This versatility could promote psychological acceptance of such devices by eliminating some of the constraints of rigidity. This wave of soft robotics has led to the introduction of soft actuators[37–40] and the possibilities of combining them to create soft continuum manipulators in various categories such as cable-driven actuators,[41,42] pneumatic artificial muscles,[43–46] inflatable structures,[47–50] and fluidic elastomeric actuators.[51–53] The blend of soft robotics and wearable manipulators sets forth a new category of robots, which we name Soft Poly-Limbs (SPL's), that is, soft manipulators that act as extra appendages.

In this article, we portray the potential of a soft and modular upper limb SPL for safely and effectively assisting the four main categories of users and tasks, as shown in Figure 1 and Supplementary Movie S1 (Supplementary Data are available online at www.liebertpub.com/soro). We present the major components of the SPL, including as follows: (1) the new design of the robust, elastomeric ring-reinforced actuators (RRAs); (2) the three-chambered actuators (3CAs), made by bundles of multiple RRAs; and (3) the complete continuum SPL. We investigate the mechanical behavior of the soft, highly articulated limb and its components by analyzing a set of design parameters using computational finite element method (FEM) models that we validate experimentally. We also address some of the concerns of possible future adopters in design, function, and esthetics of the SPL. Lastly, through a series of experiments we showcase the potential of this novel wearable robot limb by demonstrating a variety of interactions, user intention detection methods, and usage tasks between a human and the SPL. In particular, the contributions of this work are:

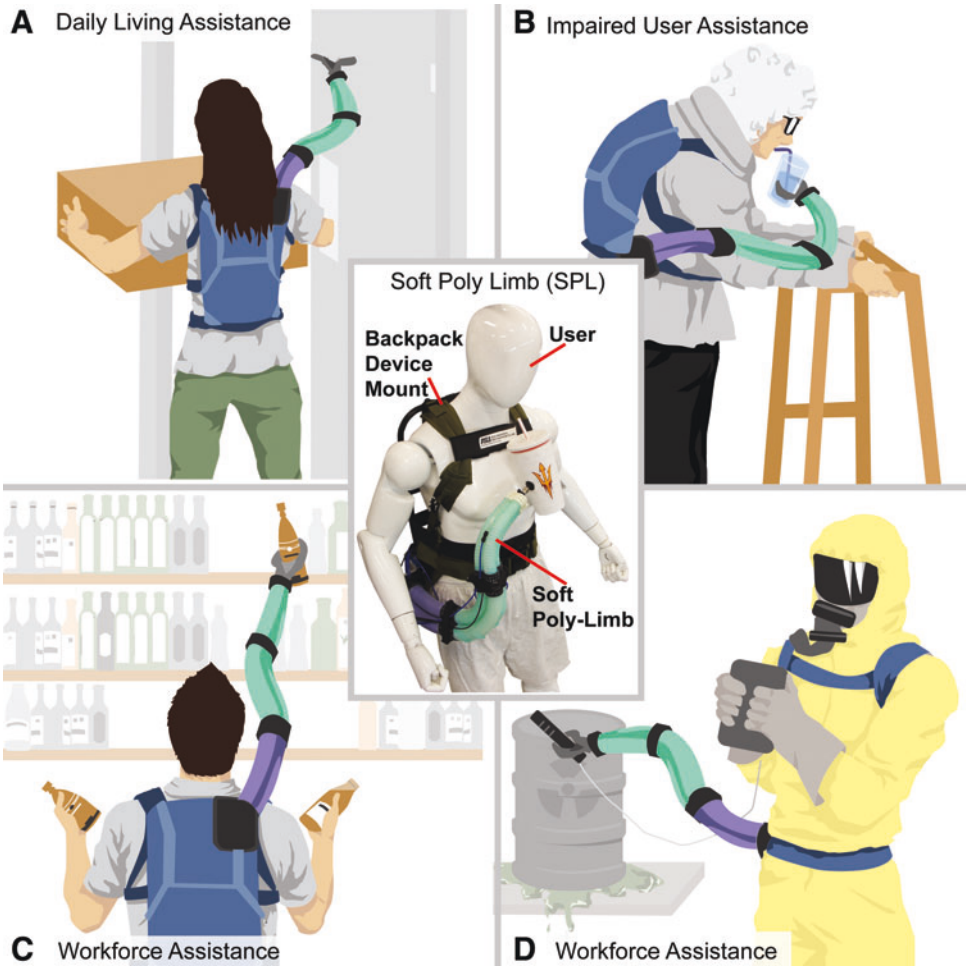

FIG. 1. Illustrations of the SPL in some of its many possible use cases. The prototype SPL (*center*) mounted on a back frame system is a soft, lightweight, wearable robot that is designed to assist users with functional tasks. **(A)** Daily living assistance: opening a door when the user's hands are full from carrying objects. **(B)** Impaired user assistance: assisting an aging user with feeding. **(C)** Workforce assistance: assisting a grocery store worker restack shelves with products quicker and access higher shelves that cannot normally be reached. **(D)** Hazardous task assistance: assisting a user measure, from safe distance, the radiation levels, and collect radioactive samples on-site. SPL, Soft Poly-Limb. Color images available online at www.liebertpub.com/soro

1. Design and development methodology of a novel SPL capable of assisting a wide range of users.
2. First-time demonstration of a soft arm mounted on a user, capable of operating by counteracting gravity in the horizontal plane.
3. A set of systematic design rules, which allows the soft robotics community to design their own SPL, that is compact, robust, and capable of highly articulated motions in three-dimensional(3D) space.
4. Investigation of the geometrical parameters of the components that make up the SPL (the novel introduction of the soft single RRAs and their bundle version, called the 3CA).
5. New quasistatic computational (FEM) models, which can accurately estimate the motion behavior of RRAs, the 3CAs, and the entire SPL under varying geometrical parameters that are validated with physical experiments and kinematic models.
6. Exploration and validation of the SPL's capability to produce high payload-to-weight ratio (2.35 times its own weight).
7. Exploration and validation of hands-on and hands-free methods of detecting user intent to perform gross and fine control of the SPL.
8. Investigation of the SPL's capabilities to safely operate and interact around a human by picking and placing daily living objects and assisting in multitasking scenarios through variable mounting positions of the SPL on the human body.

Materials and Methods

Actuator materials

Properties of the elastomeric materials are initially determined using a standard testing method, ASTM D412, which involves a uniaxial tensile strength test and curve fitting of the collected data with various hyperelastic models, such as the Yeoh,[54] Ogden,[55] and Neo-Hookean models,[55] to obtain the most accurate material property coefficients for modeling. The Yeoh,[54] Ogden,[55] and Neo-Hookean models fall into the category of phenomenological models that are created based on the descriptions of the observed material behavior.[55] These models are widely used and generally yield good results for soft hyperelastic materials.[55] Curve fitting the material data with the aforementioned models, the Ogden model demonstrated the most suitable fit using an R^2 coefficient to determine accuracy. All of the 3D FEM models are created and analyzed using ABAQUS/Standard (Simulia, Dassault Systemes) and formulated as tetrahedral quadratic hybrid elements (element type C3D10H). Models for the RRA are gauged for the maximum linear extension with a varying internal pressure in the actuator. Models for the 3CA are analyzed for the maximum bending angle with a varying internal pressure in the two adjacent actuators of the 3CA. Finally, a model for the entire SPL is analyzed for its ability to perform complex poses while utilizing all of its 3CAs.

The RRA is composed of two main components, the elastomeric actuator body and the reinforcement rings. In this study, we focus on varying the spacing between the rings and the thickness of the rings. The material of the rings is a digital acrylonitrile butadiene styrene (ABS) and is treated using an elastic model with Young's modulus of $E = 2620$ MPa and a Poisson's ratio of $\vartheta = 0.35$. The material of the elastomeric actuator body, with a shore hardness of 30A (Dragon Skin 30; Smooth-On, Inc., Macungie, PA), is modeled using a hyperelastic incompressible Ogden third model[55] with the following material coefficients obtained after uniaxial testing of dogbone samples: $\mu 1 = 1.180$, $\alpha 1 = 1.069$, $\mu 2 = 0.874$, $\alpha 2 = -1.237$, $\mu 3 = -1.939$, $\alpha 3 = 0.134$, $D1 = 0.702$, $D2 = 0$, $D3 = 0$.

Hardware overview

A custom soft robotics evaluation platform is designed to test the capabilities of individual RRAs, the 3CAs, and the SPL is shown in Figure 5D. The setup is designed to have the ability of fixing the SPL on a perforated plate that is mounted on linear stages capable of moving in both horizontal and vertical directions using motorized ball screws driven by servo motors (AKM Series; Kollmorgen, Radford, VA) and a linear drive system (MG06K; Thomson Linear, Radford, VA). The motorized configuration allows for accurate positioning of the soft components under investigation and is capable of performing dynamic experiments. To achieve pneumatic regulation, the experimental platform is equipped with 16 pressure regulators (ITV1050-21N2CL4 Pressure Regulators SMC) and 32 fast switching speed, high-flow, solenoid valves (MHE3-MS1H-3/2G-1/8-K; Festo, Esslingen, DE). These valves enable simultaneous and independent actuation of up to 16 soft actuators. The pressure regulators are attached to a pneumatic supply with a constant pressure of 0.413 MPa. Additionally, pressure sensors (PSAN-1C(P)V; Autonics, Mundelein, IL) are connected to each of the available pneumatically regulated fluidic lines to monitor the pressure in the soft actuators. All the pneumatic equipment and motors are controlled by a real-time controller (CompactRIO NI cRIO-9042; National Instruments, Inc., Austin, TX). The actuation system, control loop for each RRA is shown in Supplementary Figure S1; note that the SPL is made of nine RRAs. Motion trajectories of soft components are monitored through a dedicated motion capture system with six wide-angle, low-latency cameras (Optitrack Prime 13W; NaturalPoint, Inc., Corvallis, OR) that are mounted to the platform.

A universal testing machine (UTM) was also used (Instron 5944; Instron Corp., High Wycombe, UK) for testing the payload capacity of the SPL.

Participant study

A single healthy male adult (age, 23 years; mass, 80 kg; height, 1.85 m) participated in this study. The study was approved by the Arizona State University Institutional Review Board, and all methods were carried out in accordance with the approved study protocol with number 00007970. The participant provided written informed consent.

Fabrication method

In the first step, molds for creating tapered RRAs are fabricated using high spatial resolution rapid manufacturing 3D printers (Objet30 and Fortus250; Stratasys, Eden Prairie, MN). As shown in Figure 3A(i), the mold is comprised of

four parts: a two-part shell, a center cylindrical core, and a top cap. The two-part shell is designed with extruded features to create evenly spaced, circular impressions on the inner silicone for the alignment and placement of the reinforcement rings in the following step. The two-part shell is secured together and a silicone mixture of shore hardness 30A (Dragon Skin 30; Smooth-On, Inc.), is poured into the mold cavity. The central hollow cavity is generated using a 3D printed tapered core to ensure equal thickness of the tapered actuator wall. A dowel pin is attached to the center of the bottom end of the core to achieve the desired concentricity within the mold. A top cap is used to ensure alignment of the core and secure the core and the mold together during the silicone curing process. The mold–core setup is placed in an oven at 60°C to expedite the silicone curing process. A total of nine RRA are fabricated, three of each size for the three differently sized segments, following the same molding process.

In step two, A set of rings is 3D printed from a digital ABS material (RGD531; Stratasys) using an Objet30, 3D printer (Stratasys). The rings are designed to restrict radial expansion of the silicone actuator, allowing only axial elongation during pneumatic actuation. Each set of rings is made to fit the tapering sizing of the actuator, thus becoming incrementally smaller at each passing ring. Nine ring sets are inserted onto each soft actuator to create all the required RRAs for the SPL as shown in Figure 3A(ii).

Step three includes the fabrication of the 3CA as shown in Figure 3(iii). A two-part mold is designed to fuse the three RRAs together with the addition of a silicone core and a silicone sheath that surrounds the periphery of all actuators. The three individual RRAs, prepared in the previous step, are arranged in an equilateral triangle fashion inside the mold, offset 120° from one another, and centered using a mold cap. Liquid silicone mixture is used to fill the void space between the three RRAs and placed in an oven to accelerate the curing process. Once cured, the 3CA actuator and cores are separated from the mold. Seal tape is applied to the outer surface of the 3CA and it is dipped vertically into a shallow silicone container to simultaneously create a sealing cap in all three chambers. The seal tape prevents excess material from adhering to the actuator body. The 3CA is completed with three pneumatic lines inserted, one into each actuator, on the side with the larger segment radius.

Finally, a set of modular connections are 3D printed from a digital ABS material (RGD531; Stratasys). The connector pieces are designed to allow attachment and detachment of the modular 3CA segments using nuts and bolts. The ends of each 3CA are fitted into the connectors and the fluidic tubing line is fed through an opening in the side of the connector piece and routed loosely on the side of the actuators. The connector pieces are secured to the ends of the 3CAs with a silicone adhesive (Sil-Poxy; Smooth-On, Inc.), which ensures a strong bond between the two materials, as shown in Figure 3A(iv). All segments are then assembled creating the SPL. Any form of end effector can then be mounted at the tip of the SPL to complete the fabrication process, as shown in Figure 3A(v).

Control and characterization

To control the SPL, we developed a discretized pneumatic control scheme. As shown in Figure 7A, the low-level pneumatic control architecture linked the user intent to the physical position of the SPL. The maximum workspace of the limb and each individual 3CA segment was discretized into a 5×5 end effector motion controller. Pressurization of the SPL to the desired location is accomplished by controlling fast-switching solenoid valves to allow regulated pressure into the selected RRAs at a constant rate. This closed-loop system is monitored at a low control level with pressure sensors connected in series to each RRA. User intent is captured using an analog joystick (OM300B-M2; Yueqing Omter Electronic & Technology Co., Ltd., Wenzou, China), an inertial measurement unit (IMU) sensor (BNO055; Bosch, Broadview, IL), and a set of surface electromyography (sEMG) sensors (MyoWare AT-04-001; Advancer Technologies, Raleigh, NC).

SPL oscillations during pressurization were combated by a stepping algorithm within the control logic (Supplementary Fig. S2). To move between chosen positions, the algorithm divides the total change in pressure for each RRA by i, an iteration variable representing the number of steps, as defined by the user. The output is a constant pressure change in each RRA for every step. Each step has an experimentally calibrated delay, which provides a tradeoff between actuation speed and end-position oscillation.

Results

Design considerations for a SPL

We design and develop the modular SPL, as shown in Figure 2B. The SPL consists of three different modular segments, called the 3CAs. Each fluid-driven chamber of the 3CA is a single RRA. The RRA is a tubular soft-silicone actuator made of ring reinforcements. These rings are located along its external walls and are designed to restrain radial expansion and promote linear extension motion when pressurized (Fig. 3B). In our preliminary[56] work, we have demonstrated that grouping fiber-reinforced actuators (FRAs),[37] allowed the interacting actuators to produce a three degree of freedom (DoF) motion. However, it was noticed that the thin fiber reinforcements would slowly slice into the elastomeric body of the actuator during each pressurization cycle, eventually damaging the actuator. To improve the robustness of the reinforced actuators,[57–61] we introduce new ring reinforcements, with a larger contact surface area. These plastic ring reinforcements are quick and easy to fabricate using digital fabrication techniques and are shown to be more robust for long-term use.

Connecting three 3CAs in series, as shown in Figure 2B, produces a highly maneuverable continuum soft robotic limb with a total of nine DoFs. The length of the SPL is designed to approximately match the length of an average-sized adult male arm, which is around 0.59 m from the tip of the shoulder to the center of the wrist.[62] Each of the SPL segments has a length of 160 mm. With the inclusion of a modular connector piece in between each segment, the SPL is $\sim$0.57 m in length. Furthermore, tapering is applied to the segments and SPL, similar to that seen in arms and trunks of animals like the octopus and elephant, respectively, which utilize highly flexible and articulated tapered appendages.[63] A decreasing diameter at each segment ensures a reduction of volume and weight at the distal end, bringing the limb's center of mass closer toward the body of the user and its total weight to

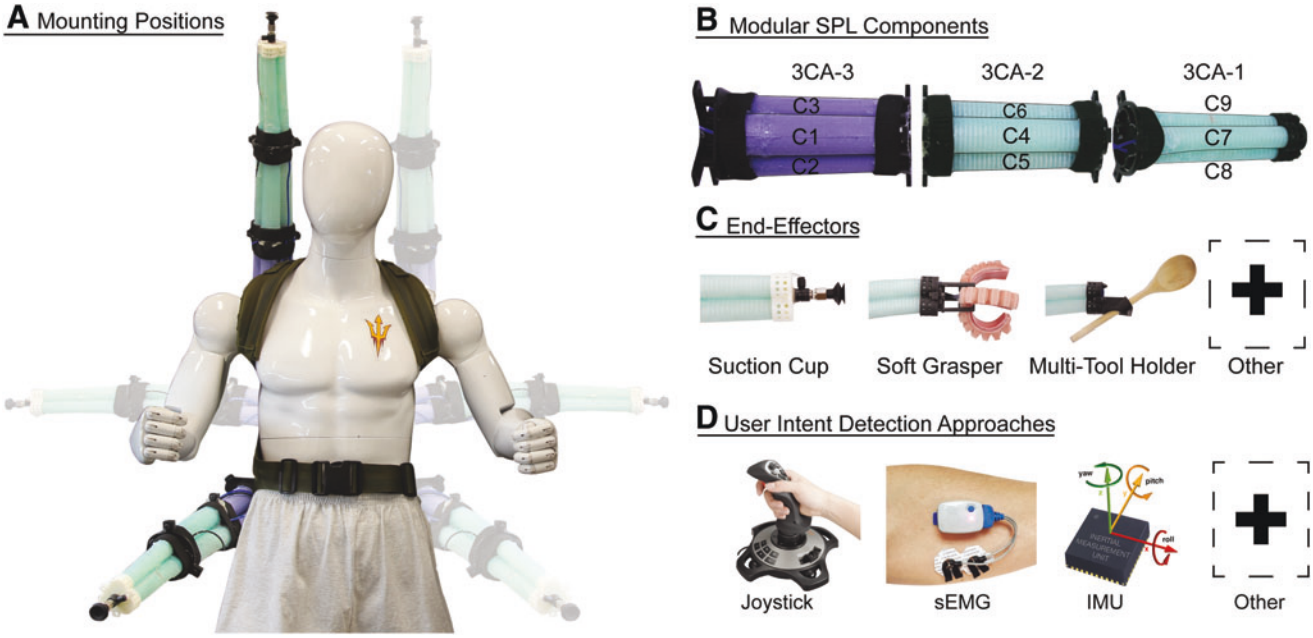

FIG. 2. Customizability and modularity features of the SPL. **(A)** The SPL allows the user to mount the limb at various positions on the back frame to enable access to different task spaces. **(B)** The SPL is constructed with three modular tapered segments, the 3CAs. Each 3CA segment is made of three elastomeric chambers placed in an equilateral triangle formation, called the RRAs. Each RRA is capable of extending axially when pressurized. The contact interactions between the extending RRAs create 3D bending motion of the segments. **(C)** The end effector of the SPL is reconfigurable depending on the end effector functional module required for the task. The entire body of the SPL can also be utilized as an end effector. **(D)** The SPL can be operated by decoding the user's intent through a variety of sensing modalities. In this work, we use a joystick controller, sEMG sensor, and IMU sensor to demonstrate mobility control of the SPL in 3D space. 3CA, three-chambered actuator; 3D, three-dimensional; IMU, inertial measurement unit; RRAs, ring-reinforced actuators; sEMG, surface electromyography. Color images available online at www.liebertpub.com/soro

1.6 kg. Additionally, the acceleration of locomotion is increased, due to an increased ratio of force over mass.[64]

Based on previous investigations with reinforced actuators, we improve and optimize the soft actuator performance accounting for input pressure and stiffness so as to achieve higher payload capacity and better motion performance.[37,56] We set the hyperelastic silicone material used in the development of the SPL to a higher shore hardness of 30A compared with previously developed actuators,[37,56] producing an overall stiffer limb, but capable of receiving higher pressure when actuating and thus achieving higher torque generation. Following the tapering angle of the limb, the wall thickness of the actuators (Fig. 3B) are set at 7 mm for the proximal segment, 6 mm, and 5 mm for the actuators in the subsequent segments. The decrease in thickness in conjunction with the tapering ensures that stiffer segments closer to the limb base are capable of supporting the weight of their neighboring segments, while gradually reducing the weight and volumetric stiffness of the actuators.

To enable better adoption of the technology, the lightweight SPL allows the user to customize esthetic and practical features, such as color, and enables its segments to detach for ease of carriage, cleaning, and maintenance. More importantly, because of the SPL's modular nature, the user can reconfigure the end effector, swapping any type of functional module required to achieve a specific task (Fig. 2C). The SPL is not limited to performing manipulation tasks with just variable end effectors. It is also capable of utilizing its entire soft body to grasp and carry objects larger in size and weight, something that traditional rigid robotic arms are incapable of achieving. Furthermore, mounting the SPL onto a comfortable back frame system, weighing only 1.47 kg, makes the don and doff process simple and similar to putting on a backpack. The back frame system also provides the user with a variety of potential mounting positions for one or multiple SPLs, as shown in Figure 2A. This allows execution of tasks, which require the SPL to reach different areas around the vicinity of the user, expanding its operational space. Finally, at a higher control level, user-intent detection methodologies are explored to enable operation of the SPL. A variety of sensing modalities are utilized, as shown in Figure 2D, from a joystick, to sEMG electrodes, and IMU. Overall, the SPL system could offer a vast range of features and configurations for the user, to enable execution of diverse activities of daily living.

Soft actuator design and optimization

To optimize the bending and payload performance of the SPL, a set of geometrical parameters, of both the RRA and 3CA, are modeled and studied. In Figure 3B, we introduce the geometrical parameters of a single RRA. The ring diameter and ring spacing are explored in detail to better understand the influence of the ring reinforcements on the tapered actuators. In Figure 3C, we introduce the geometrical parameters of the 3CA bundle, where the spacing between the actuators and the tapering angle are studied. Furthermore, new quasistatic computational (FEM) models that utilize the varying set of geometrical parameters are developed to

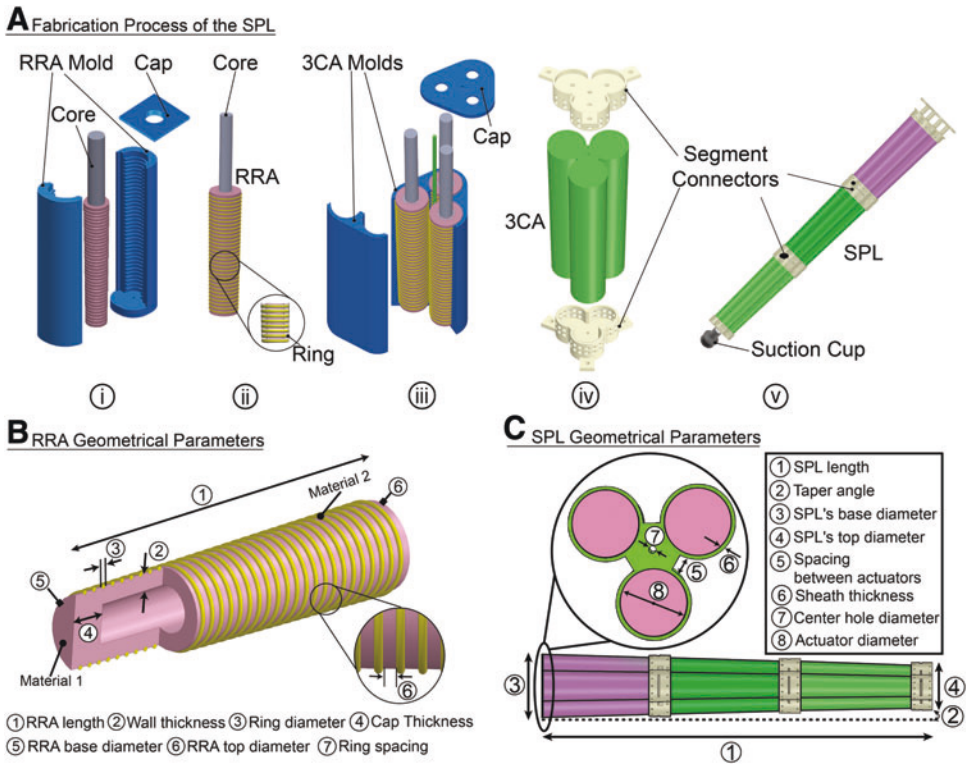

FIG. 3. Fabrication process and geometrical parameters of the SPL. **(A)** Illustration of the fabrication steps required to make the SPL: **(i)** Molding step of the single RRA using 3D printed molds. **(ii)** Manufactured thin plastic rings are inserted along the length of the actuator to create a RRA and restrict radial expansion when pressurized. **(iii)** Three RRAs are casted and angled into a mold to create the 3CA with bending abilities. **(iv)** Both ends of the 3CA are capped with a silicone cap and modular connector pieces are attached to both ends of the 3CA. **(v)** Three different-sized 3CAs are connected together to create the SPL. **(B)** Soft RRA with labeled geometrical parameters and design variables that alter its mechanical behavior when pressurized. Material 1 is the material of the elastomeric body. Material 2 is the material of the reinforcement rings. **(C)** Soft 3CA bundle with labeled geometrical parameters and design variables that affect the SPL's mechanical behavior when pressurized. Color images available online at www.liebertpub.com/soro

simulate the function of the RRAs, 3CAs, and the SPL. Prior work on FEM models for single-chambered hyperelastic actuators[37,65,66] have demonstrated their ability to provide good visualization of deformations, stress–strain concentration locations, and insights about the actuator's overall performance in free space. However, minimal work is currently observed for computational modeling of a bundle of reinforced elastomeric actuators and of a full soft-continuum arm. In this work, we introduce new, experimentally validated, FEM models that provide a realistic nonlinear analysis of the interacting bundles of hyperelastic RRAs under pressurization and loading conditions.

To optimize the performance of the soft SPL, we first investigate the effect of the number of the reinforcing rings around the silicone elastomer actuator body of the RRAs. The ring count on the surface area of the actuator is varied (Fig. 4A) following:

$$n = \frac{l}{d_r} \cdot x \tag{1}$$

where, n is the number of rings, l is the length of the actuator, d_r is the diameter of the ring cross-section, and x is the normalized ring count ratio; the ratio of the number of rings n over the maximum possible number of rings, with a diameter d_r that can fit an actuator of length, l. For example, an actuator with $l = 160$ mm, $d_r = 2$ mm, and, $x = 0.5$ yields to a ring count of 40. From Figure 4A, it is observed that under the same pressure conditions, increasing the ring count ratio from 0.125 to 0.375 results in an increase in the linear extension of the RRA. However, for ring count ratios over 0.375, the extension of the actuators demonstrates an opposite effect and decreases. This nonlinear trend indicates that at a high ring count ratio, the actuator might not be able to linearly extend at all, as the rings occupy the large portion of its surface and restrict hyperelastic stretch. Therefore, the ring count ratio used for calculating the number of rings utilized in this study is 0.375.

The second set of FEM models investigates the optimal thickness of the rings by varying their cross-sectional radius from $\frac{d_r}{2}$ mm to $3 \cdot \frac{d_r}{2}$ mm, as shown in Figure 4B. The results are used to correlate the extension of the actuator as a function of the pressure for each thickness variation showcasing that the effect in extension due to ring thickness is minimal. By setting an arbitrary number of rings ($n = 30$), simulations with varied thicknesses (from $\frac{d_r}{2}$ to $3 \cdot \frac{d_r}{2}$) are evaluated. We noticed that there are no noticeable changes in extension between the different thicknesses, as shown in Figure 4B. The number of rings (n) featured for this SPL setup is calculated using Equation 1, with $l = 160$ mm, $d_r = 2$ mm, and $x = 0.375$ mm, and resulting number of rings $n = 30$. With this resulting number of rings, the overall weight of the rings with $\frac{d_r}{2}$ and $3 \cdot \frac{d_r}{2}$ is 11.26

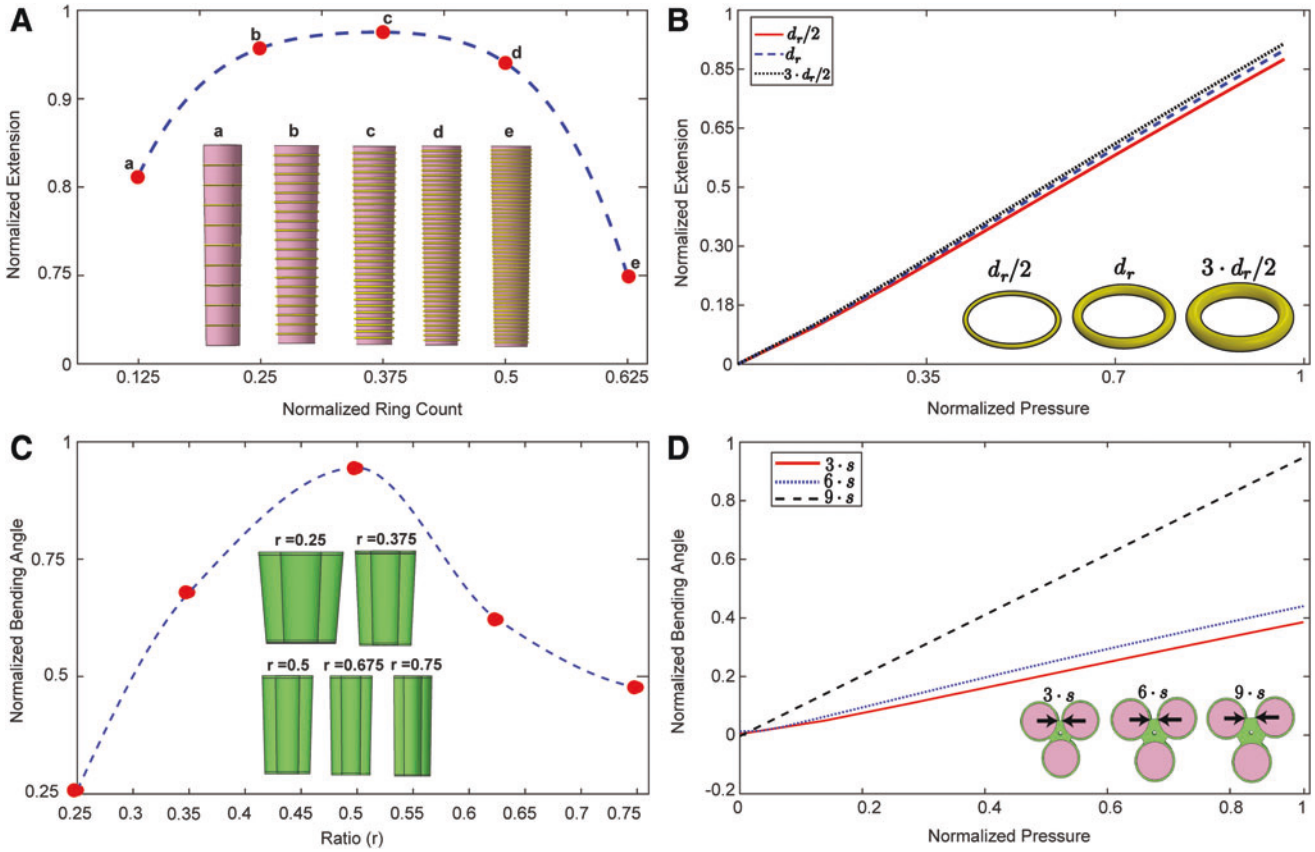

FIG. 4. Soft actuator design and optimization using computational FEM models. **(A)** Normalized extension versus normalized ring count for single RRA. Actuators are all equally pressurized. Simulations indicate that the increase in the number of rings improves the performance of an actuator only up to 0.375 ring count. **(B)** Normalized extension versus normalized pressure graph for single RRAs with different ring thickness (d_r is the cross-sectional diameter of the rings). **(C)** Angle of bending versus taper ratio (t_{ratio}), calculated in Equation 3. The graph shows five different simulated tapering ratios, 0.25, 0.375, 0.5, 0.675, and 0.75 with equal pressure. The taper 0.5 ratio demonstrates the highest bending angle. **(D)** Normalized bending angle versus normalized pressure of the 3CA with varying spacing between RRAs. Results indicate that larger spacing between actuators can generate larger bending angles with less pressurization. The *black arrows* signify the spacing in between the actuators. The $3 \cdot s$, $6 \cdot s$, and $9 \cdot s$ are the sizes of the spacing. FEM, finite element method. Color images available online at www.liebertpub.com/soro

and 11.72 g, respectively. Therefore, a ring set with cross-sectional diameter of $\frac{d_r}{2} = 1$ mm is chosen to reduce the overall manufacturing time and weight.

In the third FEM model, to maximize the bending angle of the 3CA segments in free space, we pressurized two adjacent actuators at the same pressure, to generate bending in the opposite direction (Supplementary Movie S2). In Figure 4C and D, the taper ratio and the effect of the spacing between the actuators in a 3CA configuration are explored. The tapering ratio of the SPL can be calculated as:

$$t_{ratio} = \frac{d_{distal}}{d_{proximal}} \tag{2}$$

where, t_{ratio} is the tapering ratio, d_{distal} is the distal end diameter of the single actuator of the smallest segment, and $d_{proximal}$ is the proximal end diameter of the single actuator of the largest segment. To understand and obtain the optimum tapering ratio for the actuators of the 3CA, the base and top diameter of the single segment are varied under constant pressure, as shown in Figure 4C. Five different SPL tapering ratios are explored, illustrating that when the tapering ratio increases from 0.25 to 0.5, the maximum bending angle performance improves. However, any further increase in tapering ratio above 0.5 shows a decrease in the maximum bending angle. Therefore, to achieve a maximum bending angle in our 3CA, a 0.5 tapering ratio is required.

In the final fourth set of FEM simulations, the spacing, s, between the RRAs in the 3CA formation is varied to examine how this parameter affects the bending angle performance (Fig. 4D). The spacing is varied from $3 \cdot s$ mm to $9 \cdot s$ mm, while the tapering ratio is maintained at 0.5. Figure 4C, shows that the 3CA with the RRAs spaced further apart from one another, demonstrates a higher bending angle under same pressure. We determined that the further the RRAs are spaced apart in an equilateral triangle formation, the thicker the inner silicone core of the 3CAs will become, that is, more spacing between actuators results in more material to fill the core (gap). This thicker core provides a stiffer, yet flexible, inextensible layer in the center of the 3CA. As a result, the 3CA is less likely to extend axially, as more of the pressurization

work is directed in a pure bending motion. Some drawbacks of this are the loss of the linear extension, the increase in weight and bulk, and the loss of compactness of the 3CA bundle, which is critical for ensuring that the weight of the SPL does not generate unstable motion. With the above observations in mind, the $3 \cdot s$ mm spacing is chosen for all three segments of the SPL, which sacrifices some of the bending ability at low pressures in favor of being compact and thus less prone to torsion when loaded.

Fatigue testing of ring reinforced actuators

A fatigue test is conducted to compare the operational lifetime of FRAs[37,57–61] and our newly designed RRAs. An identical test setup for both types of actuators, that is, the FRA and the new RRA, is used, where the actuators are cyclically pressurized to a safe operating pressure from 0 to 206.8 kPa. Two sets of each type of actuator with identical geometrical parameters and material properties are tested until a large deviation in pressure is detected in each one of them, which would indicate failure, as depicted in Supplementary Figure S3. The experimental results indicate that the FRAs have an average failure occurrence around 130,000 cycles, whereas the RRAs over 1,100,000 cycles. Failure in FRAs is observed at the intersection of the silicone elastomer body and the thin fiber reinforcements. The higher stress concentrations cause the fibers to slowly cut through the silicone when pressurized. This study indicates that the new RRAs have a greater operational life expectancy when compared with the FRAs. The reason for the increased life of RRAs is attributed to the larger, curved contact surface area the ring reinforcement offers, which reduces stress concentrations at the intersection of the silicone body of the actuator and the reinforcements, which is, the rings.

SPL payload capacity

To analyze the load bearing, or payload, capabilities of the SPL, two experiments are performed with the SPL positioned at a configuration that requires maximum torque to be exerted, fully extended and parallel to the ground with gravitational forces acting orthogonal to the SPL. The following experiments showcase for the first time a demonstration of a soft continuum arm mounted on a user, capable of operating by counteracting gravity in the horizontal plane. In particular, in the first experiment, the SPL's distal end is placed under the load cell of a UTM as shown in Supplementary Figure S4A. The bottom two of the three RRAs are pressurized for all segments until the limb demonstrated signs of torsion. It is noticed that the limb exhibited an average payload capacity of 9.43 N at a length of 0.55 m, that is, the maximum reach of the SPL. This is comparable to carrying a weight of almost 1 kg. In the second experiment, loads at 0.05 kg increments are placed at the end effector location of the SPL and lifted vertically to a position parallel to the ground, as shown in Supplementary Figure S4B and Supplementary Movie S3. The maximum effective payload with a suction cup acting as the end effector is experimentally determined to be 0.3 kg. The individual chamber pressure values of the 3CAs attributed to lifting the set of loads. We determined that during the first payload experiment the SPL's end effector position is constrained to move in a single plane, exerting force only upward. In contrast, during the second payload experiment the SPL is required to lift the weight in an unconstrained motion. The latter spatial motion is affected by the weight imposed on the SPL as it introduced torsional forces, which twisted the SPL's center axis creating instabilities.

To further verify the effective payload capacity of the SPL, a setup is developed where a joystick controller enables the user to pick, move, and place the loads into a rectangular box ($0.11 \times 0.13 \times 0.55$ m) positioned 0.95 m away. The results of this experiment demonstrated that the SPL is able to transfer successfully up to 0.35 kg of load from one location to the other (Supplementary Movie S3). Similar to the static experiments, this dynamic test also presented some unwanted torsion along the length of the SPL when carrying loads above 0.3 kg. However, the tasks are still able to be completed, but with some noticeable motion oscillations.

Theoretical and experimental validation of soft components

To compare the FEM model results with the experimental performance of the RRA, a linear actuator extension investigation is performed. The evaluation platform, Figure 5D, is utilized to obtain the physical extension of the actuator in quasistatic conditions. Passive reflective markers are attached to the distal and proximal ends of the RRA and its position is recorded with the aid of motion capture cameras, while the pneumatic pressure is increased in small increments. The RRA's proximal end with the wider diameter is securely mounted using a rigid fixture, facing upward in the reverse direction of the influence of gravity, similar to the FEM simulations, as shown in Figure 5B and Supplementary Movie S2. The RRA is inflated to a pressure of 206.8 kPa, while its linear extension is recorded and averaged for five different trials. Both experimental and FEM model data demonstrated similar linear extension with a maximum displacement error of 0.54% at the distal end of the actuator, and an root mean square (RMS) error on the entire extension of 5.1 mm.

An experiment to find the bending motion trajectory of a single 3CA bundle is also conducted (Fig. 5A and Supplementary Movie S2). A set of passive reflective markers are placed at the center of the distal end of the actuator as well as its proximal end, while the motion capture system is used to track the position of the markers in space. Two of the three RRAs that comprise the 3CA are pressurized at a constant quasistatic rate from 0 to 344.7 kPa. The distal position of the 3CA obtained both through the FEM simulation and the experimental data is compared, resulting in an RMS error of 2.7 mm and maximum pressure error of 4.98%. The close match of the trajectories demonstrated that the FEM model could be utilized as a good predictor of the complex motion of the 3CA.

Finally, to investigate the ability of the FEM model to predict the nonlinear motion behavior of the entire SPL, complex limb poses are experimentally generated and recorded using motion capture coordinate data points. The obtained results are compared between the FEM model and the multisegment forward kinematic model we developed, based on the piecewise constant curvature principle[51,67,68] (Supplementary Data; Supplementary Fig. S5). To obtain the experimental results, the limb is attached on a back frame and worn by a mannequin, so that the SPL projects forward from the mannequin's hip. Four sets of three markers are placed along the length of the SPL at each interconnecting segment section. Each group of markers is linked geometrically to

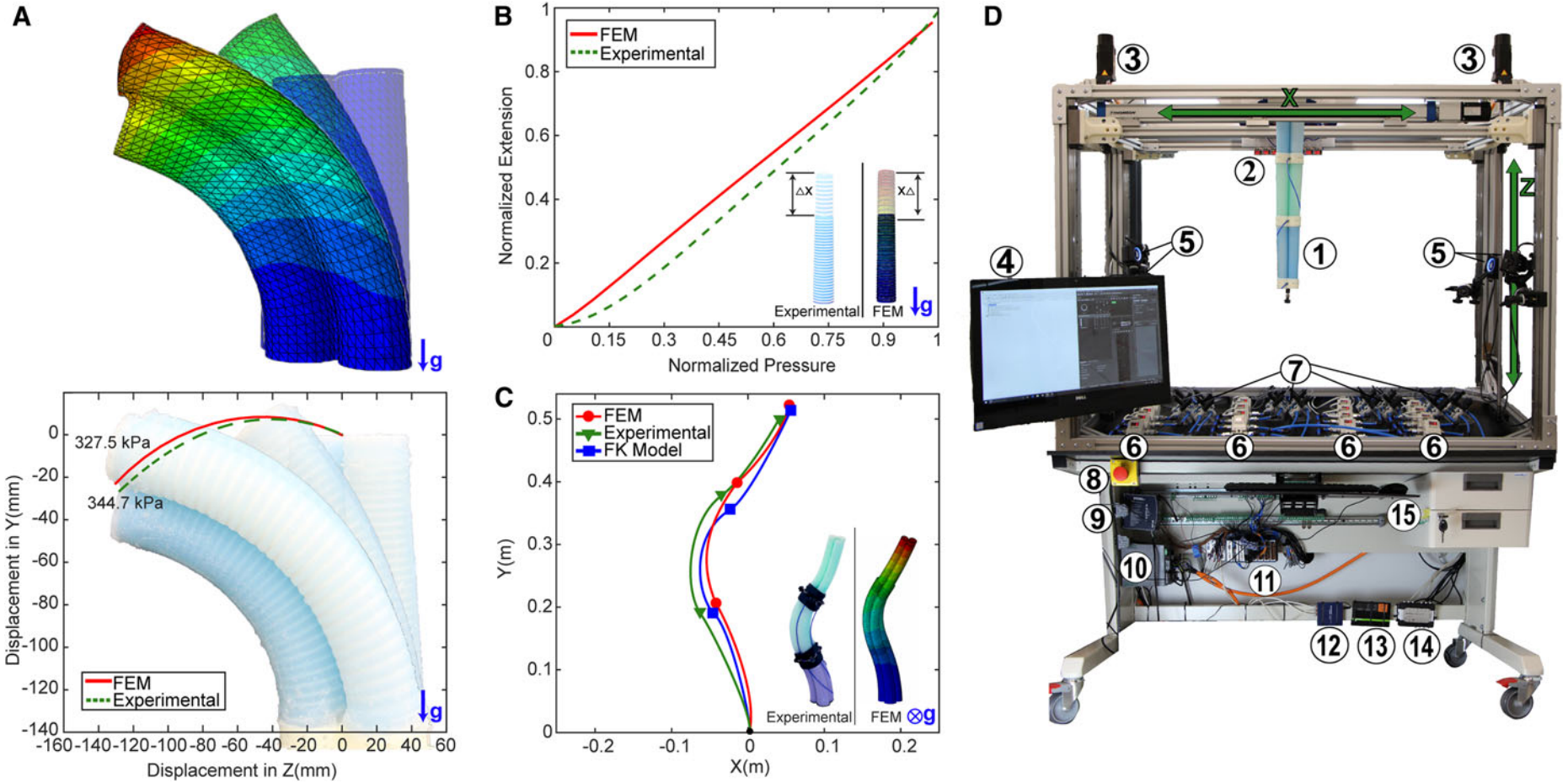

FIG. 5. Theoretical and experimental validation of soft components and the evaluation platform. **(A)** The bending 3CA actuator tip trajectory obtained from experimental results (*dotted green line*) is compared with the FEM model predictions (*solid red line*) to a pressure of 344.7 kPa. Bending configurations from both experimental and FEM are illustrated along with their overlaid tip trajectories for visual comparison. The RMS error measured between both is 2.7 mm. **(B)** The RRA extension experimental results (*dotted green line*) is compared with the FEM model prediction (*solid red line*). The RMS error between the FEM and experimental data is 5.1 mm and a maximum displacement error of 0.54% is observed at the distal end of the actuator when fully extended at 206.8 kPa. **(C)** Comparison between the end pose of the SPL as obtained from the FEM model data (*red* with *circle* markers), the experimental data (*green* with *triangle* markers), and the forward kinematics model (*blue* with *square* markers). The graph shows the top view of the SPL in a parallel configuration to the ground. The experimental Euclidean displacement error is found to be 63.3 and 25.8 mm when compared with the FEM model data and forward kinematic model data, respectively. **(D)** Experimental platform with all the equipment to monitor and control the SPL. **(1)** the SPL with a suction cup as the end effector, **(2)** digital pressure sensors, **(3)** DC servo-motors for the motion of the vertical and horizontal linear stages, **(4)** graphical user interface on a computer system, **(5)** motion capture system with six wide-angle cameras, **(6)** 16 high-speed pressure regulators, **(7)** 32 high-switching, high-flow solenoid valves, **(8)** emergency stop button, **(9)** power supplies, **(10)** DC servo-motor drivers, **(11)** real-time National Instruments Compact-Rio controller, **(12)** ethernet adapter, **(13)** 8-port Gigabit PoE/PoE+ switch for motion capture cameras, **(14)** eSync 2 box to integrate motion synchronize data with the NI system, and **(15)** keyboard and mouse. RMS, root mean square. Color images available online at www.liebertpub.com/soro

create virtual rigid bodies at the center of each segment. In one such arbitrary pose (Fig. 5C), the SPL as shown in Figure 2B, is pressurized at chamber 2 and 3 of the first segment to 345 kPa, chamber 5 and 6 of the second segment to 86 and 345 kPa, respectively, and chamber 9 of the end segment to 59 kPa. The captured SPL pose is shown in Figure 5C and Supplementary Movie S2, demonstrating that the experimental motion capture coordinates, computational FEM model results, and the forward kinematic model data (Supplementary Fig. S5), all are in good agreement. The experimental Euclidean displacement error is found to be 63.3 and 25.8 mm, when compared with the FEM model data and forward kinematic model data, respectively.

In retrospect, for the SPL with an initial, unpressurized length of 0.55 m, a maximum of 11.45% displacement error for the FEM model data, and 4.69% displacement error for the forward kinematic model data are observed. In another arbitrary pose (Supplementary Fig. S6), the SPL is pressurized at the bottom right chamber of the first segment to 345 kPa, the bottom left chamber of the first segment to 86 kPa, the bottom right chamber of the second segment to 86 kPa, the bottom left chamber of the second segment to 345 kPa, and the bottom right chamber of the last segment to 59 kPa. The calculated Euclidean displacement error is 18.89 and 49.12 mm, when compared with the FEM model data and the forward kinematic model data, respectively. This is in close agreement with our previously presented pose in Figure 5C.

SPL workspace

To evaluate the capability of the SPL to articulate about its mounted base, a workspace assessment experiment is performed. The soft limb is mounted on a back frame and worn by a human mannequin standing vertically. Using an analog joystick as the user intent control system (Fig. 2D), the SPL is manipulated to 25 predetermined locations in 3D space, which covered the observed reachable workspace of the limb. A motion capture system is used to record the position of the SPL at each of the interconnecting points of each segment. The workspace illustrated in Figure 6B and C, is shown in the top and front view, as obtained after the linear extrapolation of the collected 25 location points. From the workspace test, the measured workspace volume is calculated to be $\sim 0.08\,m^3$. The maximum reach, horizontal range, and vertical range of the SPL are 0.55, 0.69, and 0.72 m, respectively. Figure 6A and Supplementary Movie S4, show the motion of the SPL as it goes through the workspace test. It is noticed that the workspace's virtual boundaries are constrained to allow the SPL to traverse closely around the user's body without coming in contact during its traveling path, as shown in Supplementary Movie S5.

User-intent detection

We demonstrate user control of the SPL through three user-intent detection modalities, namely an analog joystick, an IMU, and a sEMG sensor. User-desired motion of the SPL is captured and processed by a 5×5 discretized motion controller (Fig. 7A). The 5×5 matrix represents the 25 reachable end effector locations in space within the workspace of the SPL. Each output location within the motion controller indicates a set of bounds for the desired intent-sensed positions. Therefore, any user-desired goal location that falls within these bounds will automatically register the limb to one of the 25 predefined locations.

User-intent detection using the joystick sensing setup is achieved through tracking the change in position of its three degrees of freedom: planar motion on the XY plane and rotation around Z (twist). Desired SPL end effector position is achieved through joystick movement along its X and Y axes. Figure 7B demonstrates an experiment, in which the joystick position is correlated to the end effector positions. A motion capture system is used to record the position of a passive reflective marker placed on the distal end of the SPL, while the position of the joystick is tracked. The observed square-shaped

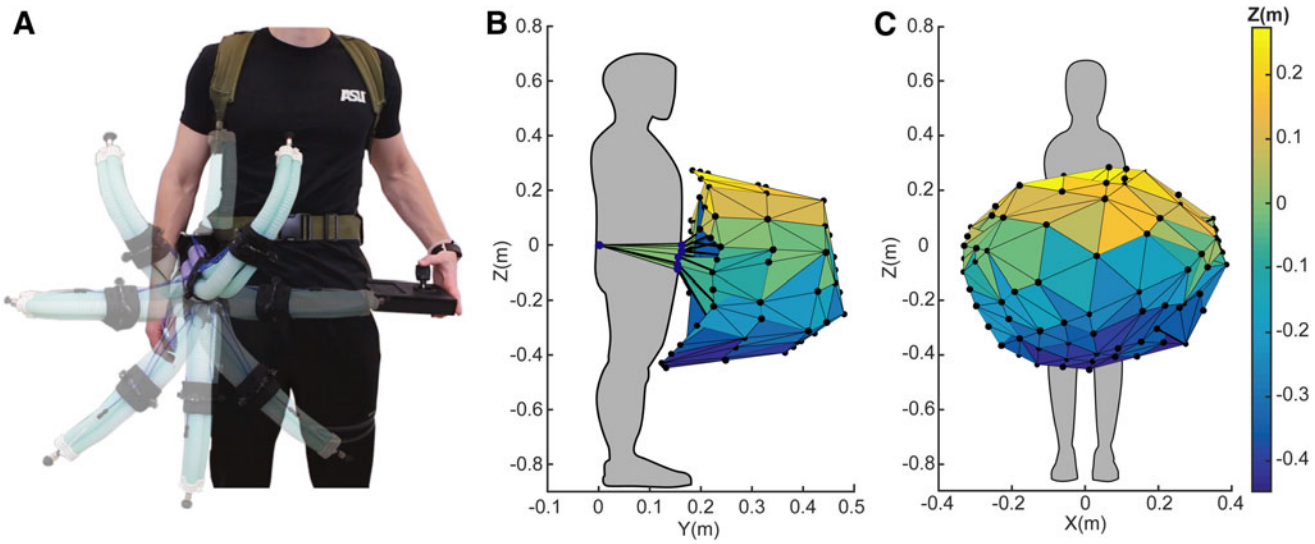

FIG. 6. Workspace of the SPL. **(A)** The SPL traversing through its maximum workspace around the user when mounted at the waist. **(B)** Side view of the workspace of the SPL. The vertical range of the SPL is 0.72 m. **(C)** Front view of the workspace of the SPL. The horizontal range of the SPL is 0.69 m and the maximum reach is 0.55 m. Color images available online at www.liebertpub.com/soro

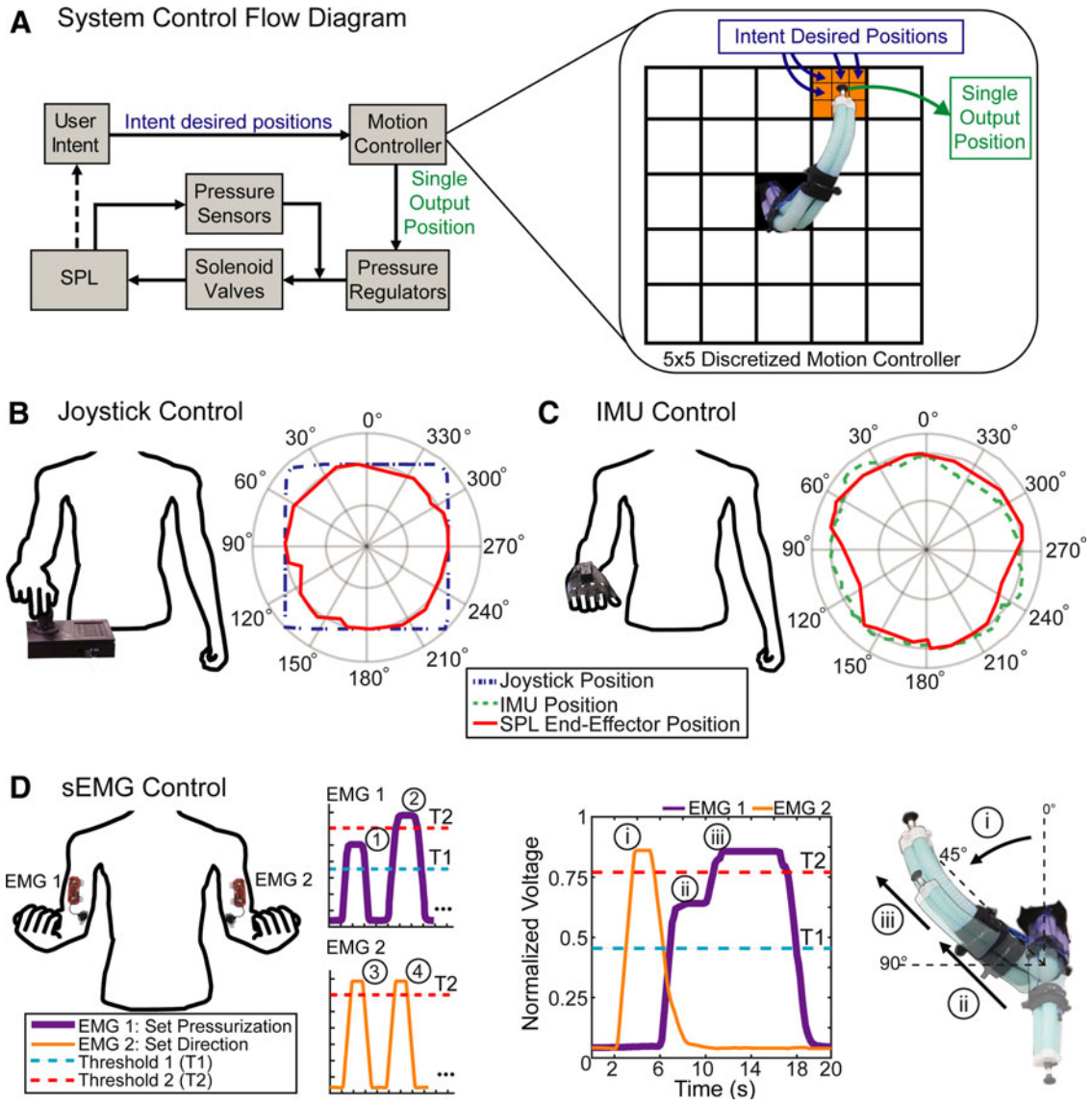

FIG. 7. User-intent detection and control. **(A)** High and low-level control flow diagram of the SPL. User intent is estimated using one of the following sensing modalities: joystick, IMU, or sEMG. User-desired position of the end effector is determined by a discretized motion controller which correlates the position of the sensor with a preset SPL pressure values obtained by a 5×5 table. Any intent-sensed position will place the controller within one of the 25 predefined positions the SP can reach. The SPL is pneumatically pressurized using a closed-loop, low-level controller that regulates the solenoid valves utilizing pressure sensors feedback. **(B)** User-intent detection and control through analog joystick. The position of the joystick (*blue line*) is compared with the position of the SPL end effector (*red line*). The observed *square* path of the joystick is due to its rudimentary, two-axes design. The joystick, however, does produce the intended circular motion of the SPL. **(C)** User-intent detection and control through IMU mounted on the dorsal side of a glove. The observed IMU position is tracked (*dotted green line*) and compared with the SPL motion (*red solid line*). **(D)** (*Left*) User-intent detection and control through sEMG sensors on both biceps brachii muscles. EMG 1 controls pressurization of SPL and EMG 2 controls direction of gross motion. **(1)** EMG 1 output between T1 and T1 pressurizes the SPL to half of its maximum pressure in the set direction of motion. **(2)** EMG 1 output above T1 pressurizes the SPL to its maximum pressure in the set direction of motion. EMG 1 output below T1 depressurizes the SPL. **(3)** EMG 2 output above T2 sets the SPL direction of motion 45° counterclockwise in the coronal plane (looking at the user). **(4)** A second EMG 2 output above T1 adds another 45° counterclockwise, that is, to a direction of 90°. Direction can be set in 45° increments around the entire 360° of motion. (*Right*) An example SPL motion is shown: **(i)** An EMG 2 activation above T2 sets the uninflated SPL's direction of motion along the 45° plane. **(ii)** An EMG 1 activation between T1 and T2 pressurizes the SPL to half of its maximum pressure in the 45° direction. **(iii)** An increased EMG 1 output above T2 pressurizes the SPL to its maximum pressure in the 45° direction, and held in position while EMG 1>T2. The release of EMG 1 below T1 depressurizes the SPL to its initial, deflated position. Color images available online at www.liebertpub.com/soro

joystick position pattern is a result of its elementary, two-axes design. Nevertheless, the joystick successfully articulated the end effector to user-desired positions (Supplementary Movie S5). In addition to gross limb motion, twisting the joystick about the Z axis enables fine motion adjustment of individual segments (Supplementary Movie S5).

User-intent detection using an IMU sensor, mounted on the dorsal side of a glove, is estimated from the change in pitch and yaw rotational angles, in addition to tactile buttons. Intent-sensed position of the SPL is directly derived from the pitch and yaw angles as these change, while the user rotates their hand toward the desired SPL direction of motion. An experiment is performed to correlate the position measured by the IMU to the position of the SPL's end effector (Fig. 7C). The position of a passive reflective marker on the distal end of the SPL is recorded using motion capture cameras, while the position of the IMU is also recorded as the user moves their hand in free space. During this tracking experiment, a circular motion of the user's hand, thus of the IMU, resulted in the end effector of the SPL following a similar circular motion (Supplementary Movie S5). Individual segment selection for finer control of the limb is achieved by pressing at two tactile buttons located on the side of the glove near the first metacarpophalangeal joint of the thumb (Supplementary Movie S5).

User-intent detection using a sEMG sensing setup is measured from the change in myoelectric impulses obtained by two sEMG sensors, each placed on one bicep brachii muscle, as shown in Supplementary Movie S5. Pressurization of the SPL is accomplished by the first sEMG sensor (EMG 1), whereas direction of the SPL motion is defined by the second sEMG sensor (EMG 2), as shown in Figure 7D. Desired limb movement is set by the amplitude of myoelectric signals in relation to two threshold values (T1 and T2), as shown in Figure 7D. When the EMG 1 signal is maintained between T1 and T2 (Fig. 7D(1)), the SPL is pressurized to half its maximum capacity in the defined direction. When the signal is maintained above T2 (Fig. 7D(2)), the SPL is pressurized to its maximum capacity in the defined direction. An EMG 1 signal below T1 depressurizes the SPL entirely. In parallel to EMG 1 signal, the amplitude of the EMG 2 signal is also monitored. When the EMG 2 signal momentarily exceeds T2 (Fig. 7D(3)), the SPL increments by 45° to a new direction angle following a counterclockwise motion in the coronal plane (facing the user). Figure 7D(4) illustrates the second successive activation causing the SPL to define a direction at 90°.

SPL interaction experiments

To further investigate the user controllability, the effective limb payload, and the versatility of the modular SPL, a vacuum suction cup manipulator unit, with a theoretical holding load of 0.86 kg, is used as the limb's end effector. The suction cup is connected to a vacuum pump, which facilitated depressurization rates of 1.42×10^{-3} m^3/s. The experiment is designed for the user to operate the SPL with the use of a manual joystick controller to grasp an object placed inside of a cup with radius and height of 0.032 and 0.11 m, respectively. Subsequently, the object is transferred with the SPL across the table along a distance of 0.95 m, and finally placed into a rectangular box ($0.11 \times 0.13 \times 0.55$ m). The combined task of actuating the SPL using the manual user-intent detection and suction manipulation is successfully performed for a variety of daily living objects, including a fork (0.015 kg), a cup (0.13 kg), an apple (0.15 kg), and a banana (0.18 kg) as shown in Figure 8A and more extensively in Supplementary Movie S6.

One key advantage of a soft continuum-type manipulator, like the SPL, is its ability to perform whole-arm grasping, similar to an elephant's trunk. Whole-arm grasping means the limb can configure its entire body to wrap and grasp a wide range of objects of different sizes and shapes. Using the limb's inherent compliance, the SPL is able to perform underactuated grasping by exploiting continuum contacts, resulting in a form of manipulation that is more robust to external disturbances. With pressurization of the SPL's segments to a maximum curvature angle of 192.3°, three different weighted objects with dissimilar material texture, shapes, and sizes are grasped, that is, a soccer ball weighing 0.43 kg, a box weighing 0.83 kg, and a backpack weighing 1.04 kg, as shown in Figure 8B and Supplementary Movie S7. It is noted that the SPL's suction end effector would not be able to carry these objects due to their volume, size, and weight. The whole-body grasping strategy succeeds by applying forces to the object around its entire perimeter and pushing it against the body of the user. By doing so, the SPL is found to be capable of holding weights up to around 3.8 kg, increasing its payload capacity by 1158% in comparison to the suction cup end effector. This experiment also demonstrated that the SPL could carry weights up to 2.35 times its own weight.

Another set of experiments demonstrated the SPL's ability to allow users to perform multiple tasks in parallel by operating the limb. In one scenario, a user carrying a box with both arms is required to also use a swipe card to unlock a door. In a first execution approach of this scenario, the user holds onto the box with their arms, while assigning the card swiping task to the SPL. After swiping the card and unlocking the door, the SPL returns the card to the user before pushing the door open. In another execution approach of the same task, the user holds the box with the SPL utilizing the whole-body grasping strategy, leaving their hands free to activate the swipe access and open the door. These scenarios are depicted in Supplementary Movie S8. Furthermore, the SPL's potential to support a user with visual impairments is demonstrated by tasking the SPL to swing a walking cane and tap the floor to provide echolocation feedback, as shown in Supplementary Movie S8.

In a final evaluation experiment, the variable mounting placements of the SPL on the back frame and its ability to modify its operating range of the limb are demonstrated. Depending on the assistance the user requires with a task, we explored the performance of the SPL when it is mounted close to the shoulder joint. For this experiment, the SPL is fixed 0.45 m above the user's waist, with the end effector pointed upward in its natural resting position. This allowed the limb's workspace zone to translate from around user's right chest to around and above the head. An example use case is shown in Figure 8C, where the SPL is assisting with holding an umbrella, hands free. As shown in Supplementary Movie S9, the SPL is able to take a hat off of the mannequin's head and then subtly place it back. In Supplementary Movie S9, multitasking assistance is achieved with the SPL reaching for an object on a shelf above the user's head, while the same user performs another task. This demonstration allows us to look ahead and experiment with the SPL's capabilities when placed at different body positions, as well as provides insights that can eventually

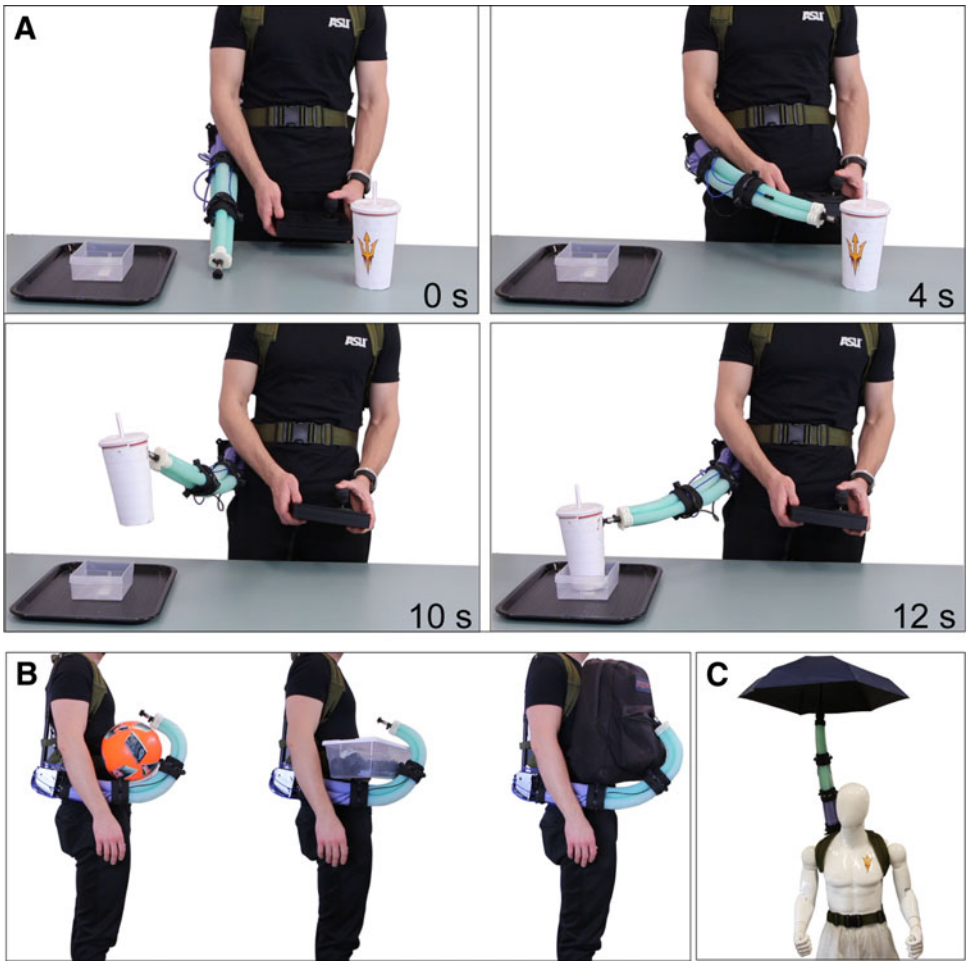

FIG. 8. Diverse grasping strategies with the SPL are available to the users. **(A)** Series of frames captured showing the SPL picking up a cup, weighing 0.13 kg, and placing it into a box. **(B)** Side view of the SPL performing the whole-arm grasping strategy with a ball (0.43 kg), a box (0.83 kg), and a bag (1.04 kg). **(C)** SPL performing overhead manipulations holding an umbrella (0.25 kg). Color images available online at www.liebertpub.com/soro

allow us to develop multi-SPL systems, that is, a system of more than one SPL on the same user.

Conclusion and Future Work

This article presented the design, computational analysis, development, and evaluation of the SPL. The vision of this work was geared toward assisting healthy and impaired individuals by offering additional soft robotic limbs, which can be mounted on the user's body to assist with activities of daily living and work-related tasks. Toward this goal, we developed a new highly articulated robotic limb, mounted on a user, capable of operating horizontally against gravity, which offers: continuum and compliant motion, a configurable design, as well as fits into the user adoption criteria, namely being personalizable, lightweight, safe, modular, and easy to don and doff.[4,24]

In particular, we introduced the design considerations and multistep fabrication process of the soft components that comprise the SPL, including the novel RRAs, which were bundled together to create the 3CA. To optimize their design we identified and introduced a set of parameters, which affect the mechanical performance of the soft components, as well as the SPL's behavior and flexibility. Quasistatic computational and kinematic models were created and utilized throughout the study, to simulate the function of the RRAs, 3CAs, and the entire SPL, with the variance of selected geometrical parameters. These parameters allowed for an optimized design of the limb, focusing on maximum bending ability, compactness, and payload. The accuracy of the computational and forward kinematic models was also experimentally validated, to provide design guidelines that the soft robotics community can utilize to create scalable and modular SPLs. Furthermore, a fatigue test was performed on the FRAs and the newly introduced RRAs, to explicitly consider the failure modes after long periods of operation, thus demonstrating the robustness of operation for the RRAs.

The SPL design took into consideration, the effect of the weight of the multidistal, 3CA segments, by varying the tapering angle of the limb to reduce the weight at each segment and by increasing the robustness of the SPL's components to hold higher pressures. This successful implementation of the SPL, lead to the development of highly compact, compliant, robotic limb with a high payload-to-weight ratio. We demonstrated the SPL's ability to maneuver in space with a series of payload and pick-and-place experiments, with different daily objects. Although the static end effector payload of the SPL was $\sim$0.96 kg, its effective end effector payload was limited to around 0.3 kg, by the effects of torsion observed in the soft limb when operating in free space. Employing the whole-body grasping strategy where the SPL wraps around the object it is manipulating, enabled lifting loads 2.35 times greater than its own body weight, measured at 1.6 kg.

We provide a scalable design framework and computational models to choose the parameters based on the application at

hand, range of motion, and payload capability. To improve the payload capacity of the SPL one can alter the overall stiffness of the SPL, while still allowing compliance in bending motion. This can be achieved by increasing the material stiffness (material properties) of the SPL and/or the amount of fluidic pressure provided, and/or thickness of the actuator's chamber walls. Another approach would be to scale up the form factor of the SPL. This would however increase the actuation pressure and most likely the weight of the arm in favor of lifting heavier objects, for example, the case for industrial applications where heavier loads are manipulated.

As previously mentioned, the torsional effects observed when carrying loads against gravity reduce the effective end effector payload of the SPL. This occurs when the SPL is loaded and therefore tends to rotate about its main, center axis. To reduce this, we have looked into added restraining components to the central core of each segment. The trade-off of these restraints is that they reduce the bending range of motion of each segment. Thus, one needs to consider the trade-offs between achieving high payloads and wide range of motion.

Additionally, the SPL was capable of maneuvering within a large configuration space that enabled safe interaction with the user and its environment. The modular design of the SPL allowed interchangeable segments for customization or swapping in case of failure. It also enabled interchangeable end effectors, such as a suction cup, soft grasper, or a custom-made tool holder. Furthermore, we demonstrated that the lightweight backpack frame allowed for potential SPL mounting placements on the user's body, providing access to various workspaces and assisting with different tasks. In this work, the SPL was used in two separate positions. The first position was at the waist level of the user; this was so that the arm was mounted closer to the center of the mass of the user. Additionally, this position was chosen so that the SPL could access space in front of the wearer, which is the typical space where activities of daily living tasks are performed. This position also allows the SPL to interact in cooperation with the user without getting in the way of the biological limbs. The second position was over the right shoulder of the user, and this was tested to provide insight into the difference in mounting locations and demonstrate over the head of the wear manipulation. In the future, further efforts will be made to explore the workspaces of multimounting positions and the idea of many interacting SPLs on one user.

The potential of performing multitasking assistance was explored in various test scenarios, such as opening a door when the user had their hands full, or picking an object from a shelf while performing another task. These demonstrations illustrated the SPL's capability of successfully carrying out different daily living tasks. However, these complex experiments were performed with the help of an external user controlling the SPL. Future work will further seek to improve, and possibly integrate, one or more hands-free forms of user-intent detection to support SPL multitasking assistance with the volition of the user.

We also explored various forms of user-intent detection (joystick, IMU, and sEMG sensors), to control the SPL with the user's volition. In particular, a discretized control methodology enabled the user-intent signals to successfully be mapped into real-world coordinates that operate the SPL within its workspace. In addition, to achieve fine regulation of the SPL's motion, the user was able to further control each segment individually. The current limitation of using the joystick and IMU-sensing approaches was that it required the use of at least one hand. On the contrary, the sEMG approach, offered a hands-free controlling of the limb, but requires further exploration to enable control of individual segments.

One major limitation of the SPL on real-world viability is the fact that the system is currently tethered. Focusing on this, we plan to explore a decentralized and distributed onboard actuation system and power supply, while investigating soft sensing technologies that can be embedded at each segment. This approach will allow us to measure the curvature and pose of the SPL in real-time without the indoor restriction imposed from a motion capture system.

Finally, we will look into solving the dynamic instabilities observed through preliminary evaluations, when the SPL's acceleration is fast or repetitive in nature. The inertia produced by the many passively following segments of the SPL lead to significant oscillations and therefore need to be modeled to offer more stable motion profiles. We plan to explore the control of the SPL using distributed sensing and control techniques to allow the SPL to generate its own continuum motion rules to achieve a task.[69] Overall, we are firm believers that this work will provide the gateway to the development of a series of wearable, soft, and lightweight poly-limbs that can interact and assist the healthy, as well as the impaired, with versatile tasks at work environments and activities of daily living.

Acknowledgments

This work was supported in part by the National Science Foundation under Grant CMMI-1800940. The authors thank S. Sridar for help with the design of the fatigue experiment, the mounting mechanism of the Soft Poly-Limb (SPL), the help provided in earlier design versions of the SPL, various help during filming, the building of the experimental platform, and providing constructive feedback. The authors thank Q. Lam for helping the design and building of the experimental platform. They thank C. Thalman for the art sketches of the first figure. They thank E. Fernandez in assisting with the designing and fabrication of three-dimensional printed molds.

Author Disclosure Statement

The authors have no conflicts of interest or competing financial interests to disclose.

References

1. Bogue R, Bogue R. Exoskeletons and robotic prosthetics: a review of recent developments. Ind Robot Int J Robot Res Appl 2009;36:421–427.
2. Gopura RA, Kiguchi K, Bandara DSV. A brief review on upper extremity robotic exoskeleton systems. In: 2011 6th International Conference on Industrial and Information Systems. Kandy, Sri Lanka, August 16, 2011, pp. 346–351.
3. Parietti F, Asada HH. Supernumerary Robotic Limbs for aircraft fuselage assembly: body stabilization and guidance by bracing. In 2014 IEEE International Conference on Robotics and Automation (ICRA), Hong Kong, China, 2014, pp. 1176–1183.
4. Vatsal V, Hoffman G. Wearing your arm on your sleeve: studying usage contexts for a wearable robotic forearm. In 2017 26th IEEE International Symposium On Robot and Human Interactive Communication, Lisbon, Portugal, 2017, pp. 974–980.

5. Kurek DA, Asada HH. The MantisBot: design and impedance control of supernumerary robotic limbs for near-ground work. In 2017 IEEE International Conference on Robotics and Automation (ICRA), Singapore, 2017, pp. 5942–5947.
6. Parietti F, Chan KC, Hunter B, *et al.* Design and control of supernumerary robotic limbs for balance augmentation. In 2015 IEEE International Conference on Robotics and Automation (ICRA), Seattle, WA, 2015, pp. 5010–5017.
7. Hussain I, Salvietti G, Spagnoletti G, *et al.* A soft supernumerary robotic finger and mobile arm support for grasping compensation and hemiparetic upper limb rehabilitation. Rob Auton Syst 2017;93:1–12.
8. Wu FY, Asada HH. ''Hold-and-manipulate'' with a single hand being assisted by wearable extra fingers. Proc IEEE Int Conf Robot Autom 2015;2015:6205–6212.
9. Tiziani L, Hart A, Cahoon T, *et al.* Empirical characterization of modular variable stiffness inflatable structures for supernumerary grasp-assist devices. Int J Rob Res 2017;36: 1391–1413.
10. Wu FY, Asada HH. Implicit and intuitive grasp posture control for wearable robotic fingers: a data-driven method using partial least squares. IEEE Trans Robot 2016;32:176–186.
11. Guterstam A, Petkova VI, Ehrsson HH. The illusion of owning a third arm. PLoS One 2011;6:1–11.
12. Tsakiris M, Carpenter L, James D, *et al.* Hands only illusion: multisensory integration elicits sense of ownership for body parts but not for non-corporeal objects. Exp Brain Res 2010;204:343–352.
13. Salvietti G, Hussain I, Cioncoloni D, *et al.* Compensating hand function in chronic stroke patients through the robotic sixth finger. IEEE Trans Neural Syst Rehabil Eng 2017;25: 142–150.
14. Parietti F, Asada HH. Independent, voluntary control of extra robotic limbs. In 2017 IEEE International Conference on Robotics and Automation (ICRA), Singapore, 2017, pp. 5954–5961.
15. Sasaki T, Saraiji MY, Fernando CL, *et al.* MetaLimbs. ACM SIGGRAPH 2017 Posters—SIGGRAPH'17 2017;1:1–2.
16. Hochberg LR, Bacher D, Jarosiewicz B, *et al.* Reach and grasp by people with tetraplegia using a neurally controlled robotic arm. Nature 2012;485:372–375.
17. Ajoudani A, Godfrey S, Bianchi M, *et al.* Exploring teleimpedance and tactile feedback for intuitive control of the Pisa/IIT SoftHand. IEEE Trans Haptics 2014;7:203–215.
18. Maheu V, Archambault PS, Frappier J, *et al.* Evaluation of the JACO robotic arm: clinico-economic study for powered wheelchair users with upper-extremity disabilities. IEEE Int Conf Rehabil Robot 2011;2011:4–6.
19. Bassily D, Georgoulas C, Güttler J, *et al.* Intuitive and adaptive robotic arm manipulation using the leap motion controller. In ISR/Robotik 2014; 41st International Symposium on Robotics, Munich, Germany, 2014, pp. 78–84.
20. Verma S, Khanna M, Tripathi VN, *et al.* Occurrence of polymelia in a female child. J Clin Imaging Sci 2013;3:18.
21. Tubbs RS, Ditty B, Bosmia ANAN, *et al.* Ischiopagus and diprosopus in India: two pairs of conjoined twins perceived as incarnations of Hindu deities. J Relig Health 2015;54:87–92.
22. Hanley EN, Stanitski CL. Incomplete congenital duplication of a lower extremity. A case report. J Bone Joint Surg Am 1980;62:479–481.
23. Bisneto ENF. Congenital deformities of the upper limbs. Part II: failure of formation and duplications. Rev Bras Ortop (English Ed.) 2013;48:3–10.
24. Al Sada M, Khamis M, Kato A, *et al.* Challenges and opportunities of supernumerary robotic limbs. In Proceedings of the CHI 2017 Workshop on Amplification and Augmentation of Human Perception, Denver, CO, 2017.
25. del-Ama AJ, Koutsou AD, Moreno JC, *et al.* Review of hybrid exoskeletons to restore gait following spinal cord injury. J Rehabil Res Dev 2012;49:497.
26. Polygerinos P, Correll N, Morin SA, *et al.* Soft robotics: review of fluid-driven intrinsically soft devices; manufacturing, sensing, control, and applications in human–robot interaction. Adv Eng Mater 2017;19:e201700016.
27. Rus D, Tolley MT. Design, fabrication and control of soft robots. Nature 2015;521:467–475.
28. Laschi C, Mazzolai B, Cianchetti M. Soft robotics: technologies and systems pushing the boundaries of robot abilities. Sci Robot 2016;1:eaah3690.
29. Carmel M, Majidi C. Soft robotics: a perspective—current trends and prospects for the future. Soft Robot 2014;1:5–11.
30. Simpson CS, Okamura AM, Hawkes EW. Exomuscle: an inflatable device for shoulder abduction support. In 2017 IEEE International Conference on Robotics and Automation (ICRA), Singapore, 2017, pp. 6651–6657.
31. Ding Y, Kim M, Kuindersma S, *et al.* Human-in-the-loop optimization of hip assistance with a soft exosuit during walking. Sci Robot 2018;3:eaar5438.
32. Polygerinos P, Lyne S, Wang Z, *et al.* Towards a soft pneumatic glove for hand rehabilitation. In 2013 IEEE/RSJ International Conference on Intelligent Robots and Systems, Tokyo, Japan, 2013, pp. 1512–1517.
33. Sridar S, Qiao Z, Muthukrishnan N, *et al.* Development of a soft-inflatable exosuit for knee rehabilitation. In 2017 IEEE/RSJ International Conference on Intelligent Robots and Systems (IROS), Vancouver, BC, 2017, pp. 1–6.
34. Oguntosin V, Harwin WS, Kawamura S, *et al.* Development of a wearable assistive soft robotic device for elbow rehabilitation. In 2015 IEEE International Conference on Rehabilitation Robotics (ICORR), Singapore, 2015, pp. 747–752.
35. Park YL, Chen BR, Pérez-Arancibia NO, *et al.* Design and control of a bio-inspired soft wearable robotic device for ankle-foot rehabilitation. Bioinspir Biomim 2014;9:16007.
36. Xiloyannis M, Cappello L, Binh KD, *et al.* Design and preliminary testing of a soft exosuit for assisting elbow movements and hand grasping. In Converging Clinical and Engineering Research on Neurorehabilitation II: proceedings of the 3rd International Conference on NeuroRehabilitation (ICNR2016), October 18–21, 2016, Segovia, Spain (Ibáñez J, González-Vargas J, Azorín JM, Akay M, Pons JL, Eds), volume 15, Springer International Publishing, 2017, pp. 557–561.
37. Polygerinos P, Wang Z, Overvelde JTB, *et al.* Modeling of soft fiber-reinforced bending actuators. IEEE Trans Robot 2015;31:778–789.
38. Klute GK, Czerniecki JM, Hannaford B. McKibben artificial muscles: pneumatic actuators with biomechanical intelligence. In 1999 IEEE/ASME International Conference on Advanced Intelligent Mechatronics (Cat. No. 99TH8399), Atlanta, GA, 1999, pp. 1–6.
39. Niiyama R, Rus D, Kim S. Pouch Motors: printable/inflatable soft actuators for robotics. In 2014 IEEE International Conference on Robotics and Automation (ICRA), Hong Kong, China, 2014, pp. 6332–6337.
40. Li S, Vogt DM, Rus D, *et al.* Fluid-driven origami-inspired artificial muscles. Proc Natl Acad Sci USA 2017;114:13132–13137.

41. McMahan W, Jones BA, Walker ID. Design and implementation of a multi-section continuum robot: Air-Octor. In 2005 IEEE/RSJ International Conference on Intelligent Robots and Systems, Edmonton, Alta, Canada, 2005, pp. 2578–2585.
42. Calisti M, Giorelli M, Levy G, *et al.* An octopus-bioinspired solution to movement and manipulation for soft robots. Bioinspir Biomim 2011;6:36002.
43. Walker ID, Dawson DM, Flash T, *et al.* Continuum robot arms inspired by cephalopods. SPIE Conf Unmanned Gr Veh Technol 2005;5804:303–314.
44. Godage IS, Medrano-Cerda GA, Branson DT, *et al.* Dynamics for variable length multisection continuum arms. Int J Rob Res 2016;35:695–722.
45. Ansari Y, Manti M, Falotico E, *et al.* Towards the development of a soft manipulator as an assistive robot for personal care of elderly people. Int J Adv Robot Syst 2017; 14:1729881416687132.
46. Giannaccini ME, Xiang C, Atyabi A, *et al.* Novel design of a soft lightweight pneumatic continuum robot arm with decoupled variable stiffness and positioning. Soft Robot 2018;5:54–70.
47. Sanana S. Soft Inflatable Robots for Safe Physical Human Interaction. Pittsburgh, PA: Carnegie Mellon University, 2013.
48. Hawkes EW, Blumenschein LH, Greer JD, *et al.* A soft robot that navigates its environment through growth. Sci Robot 2017;2:1–8.
49. Best CM, Gillespie MT, Hyatt P, *et al.* A new soft robot control method: using model predictive control for a pneumatically actuated humanoid. IEEE Robot Autom Mag 2016; 23:75–84.
50. Ohta P, Valle L, King J, *et al.* Design of a lightweight soft robotic arm using pneumatic artificial muscles and inflatable sleeves. Soft Robot 2018;5:204–215.
51. Cianchetti M, Ranzani T, Gerboni G, *et al.* STIFF-FLOP surgical manipulator: mechanical design and experimental characterization of the single module. In 2013 IEEE/RSJ International Conference on Intelligent Robots and Systems, Tokyo, Japan, 2013, pp. 3576–3581.
52. Marchese AD, Rus D. Design, kinematics, and control of a soft spatial fluidic elastomer manipulator. Int J Rob Res 2015;35:840–869.
53. Robertson MA, Paik J. New soft robots really suck: vacuum-powered systems empower diverse capabilities. Sci Robot 2017;2:1–12.
54. Yeoh OH. Some forms of the strain energy function for rubber. Rubber Chem Technol 1993;66:754–771.
55. Moseley P, Florez JM, Sonar HA, *et al.* Modeling, design, and development of soft pneumatic actuators with finite element method. Adv Eng Mater 2016;18:978–988.
56. Nguyen PH, Sridar S, Zhang W, *et al.* Design and control of a 3-chambered fiber reinforced soft actuator with off-the-shelf stretch sensors. Int J Intell Robot Appl 2017;1:342–351.
57. Connolly F, Walsh CJ, Bertoldi K. Automatic design of fiber-reinforced soft actuators for trajectory matching. Proc Natl Acad Sci USA 2017;114:51–56.
58. Bishop-Moser J, Kota S. Design and modeling of generalized fiber-reinforced pneumatic soft actuators. IEEE Trans Robot 2015;31:536–545.
59. Suzumori K, Iikura S, Tanaka H. Development of flexible microactuator and its applications to robotic mechanisms. Proc 1991 IEEE Int Conf Robot Autom 1991;2:1622–1627.
60. Hawkes EW, Christensen DL, Okamura AM. Design and implementation of a 300% strain soft artificial muscle. In 2016 IEEE International Conference on Robotics and Automation (ICRA), Stockholm, Sweden, 2016, pp. 4022–4029.
61. Robertson MA, Sadeghi H, Florez JM, *et al.* Soft Pneumatic Actuator Fascicles for High Force and Reliability. Soft Robot 2017;4:23–32.
62. Plagenhoef S, Evans FG, Abdelnour T. Anatomical data for analyzing human motion. Res Q Exerc Sport 1983;54: 169–178.
63. Kier WM, Smith KK. The biomechanics of movement in tongues and tentacles. J Biomech 1983;16:292–293.
64. Charles JP, Cappellari O, Spence AJ, *et al.* Musculoskeletal geometry, muscle architecture and functional specialisations of the mouse hindlimb. PLoS One 2016;11:e0147669.
65. Agarwal G, Besuchet N, Audergon B, *et al.* Stretchable materials for robust soft actuators towards assistive wearable devices. Sci Rep 2016;6:34224.
66. Connolly F, Polygerinos P, Walsh CJ, *et al.* Mechanical programming of soft actuators by varying fiber angle. Soft Robot 2015;2:26–32.
67. Godage IS, Guglielmino E, Branson DT, *et al.* Novel modal approach for kinematics of multisection continuum arms. IEEE Int Conf Intell Robot Syst 2011;10:1093–1098.
68. Webster RJ, Jones BA. Design and kinematic modeling of constant curvature continuum robots: a review. Int J Rob Res 2010;29:1661–1683.
69. Zhang W, Polygerinos P. Distributed planning of multi-segment soft robotic arms. In American Control Conference (ACC 2017), Milwaukee, WI, June 2018.

Address correspondence to:
Panagiotis Polygerinos
The Polytechnic School
Ira A. Fulton Schools of Engineering
Arizona State University
Mesa, AZ 85212

E-mail: polygerinos@asu.edu